





**Exceptional point in a degenerate system made of a gyrator and two unstable resonators**Kasra Rouhi <sup>1</sup>, Alireza Nikzamir <sup>1</sup>, Alexander Figotin <sup>2</sup>, and Filippo Capolino <sup>1,\*</sup><sup>1</sup>*Department of Electrical Engineering and Computer Science, University of California, Irvine, California 92697, USA*<sup>2</sup>*Department of Mathematics, University of California, Irvine, California 92697, USA*

(Received 11 October 2021; accepted 17 February 2022; published 29 March 2022)

We demonstrate that a circuit comprising two unstable LC resonators coupled via a gyrator supports an exceptional point of degeneracy (EPD) with purely real eigenfrequency. Each of the two resonators includes either a capacitor or an inductor with a negative value, showing a purely imaginary resonance frequency when not coupled to the other via the gyrator. With external perturbation imposed on the system, we show analytically that the resonance frequency response of the circuit follows the square-root dependence on perturbation, leading to possible sensor applications. Furthermore, the effect of small losses in the resonators has been investigated, and we show that losses lead to instability. In addition, the EPD occurrence and sensitivity are demonstrated by showing that the relevant Puiseux fractional power series expansion describes the eigenfrequency bifurcation near the EPD. The EPD has the great potential to enhance the sensitivity of a sensing system by orders of magnitude.

DOI: [10.1103/PhysRevA.105.032214](https://doi.org/10.1103/PhysRevA.105.032214)**I. INTRODUCTION**

An exceptional point of degeneracy (EPD) is a point in parameter space at which the eigenmodes of the circuit, namely, the eigenvalues and the eigenvectors, coalesce simultaneously [1–9]. As the remarkable feature of an EPD is the strong full degeneracy of at least two eigenmodes, as mentioned in Ref. [10], the significance of referring to it as a “degeneracy” is here emphasized, hence including “D” in the EPD. An EPD in the system is reached when the system matrix is similar to a matrix that contains a nontrivial Jordan block. EPD-induced sensitivity according to the concept of parity-time (PT) symmetry in multiple coupled resonators has been studied [11–13]. Also, the electronic circuits with EPD based on PT symmetry have been expressed in Refs. [14,15] and then developed more in Refs. [16,17], where the circuits are made of two coupled resonators with gain-loss symmetry and a proper combination of parameters leads to an EPD. Primarily, it has been confirmed that the eigenvalues bifurcation feature at EPD can significantly increase the effect of external perturbation; namely, the sensitivity of resonance frequency to component value perturbations can be enhanced. Moreover, frequency splitting happens at degenerate frequencies of the system where eigenmodes coalesce, and this feature at EPDs has been investigated to conceive a new generation of sensors [18–21]. The resulting perturbation leads to a shift in the system resonance frequency that can be recognized and measured using the proper measurement setup [18]. When a second-order EPD at which specifically two eigenstates coalesce is subjected to a small external perturbation, the resulting eigenvalue splitting is proportional to the square root of the external perturbation value, which is bigger than the case of linear

splitting for conventional degeneracies [22]. The concept of EPD has been employed in various sensing schemes such as optical microcavities [13], optical microdisk [23], electron beam devices [24], mass sensors [25], and bending curvature sensors [26].

The gyrator is a two-terminal network in which the transmission phase shift in one direction differs by  $\pi$  from the transmission phase shift in the reverse direction [27]. Another property of the gyrator network is that of impedance inversion. The inductance at the output of the gyrator is observed as capacitance at the input port, and a voltage source is transformed to a current source. A relevant alias for the gyrator might be the “dualizer” since it can interchange current and voltage roles and turns an impedance into its dual [28]. Gyrators could be designed directly as integrated circuits [29,30]. Also, many operational-amplifier (opamp) gyrator circuits have been proposed [31–33], which can be classified into two types: (i) three-terminal gyrator circuits in which both ports are grounded [31], and (ii) four-terminal gyrator circuits in which the output port is floating [32,33]. Because of the availability of different realizable circuits for gyrators and their versatility as practical circuit devices, gyrator-based circuits may form an essential part of integrated circuit technology in a wide range of applications.

In this paper, we study the second-order EPDs in a gyrator-based sensing circuit as shown in Fig. 1 and explore its enhanced sensitivity (variation in the sensor’s resonance frequencies to external perturbations) and its potential for sensing devices in the vicinity of the EPD. At the EPD, the degeneracy is in both the real and the imaginary parts of the eigenvalues, as well as in the eigenvectors. Two series LC resonators are coupled in the utilized circuit via an ideal gyrator, as explained in Ref. [34]. Contrary to the study in Ref. [34], this paper demonstrates the conditions to get the EPD with real eigenfrequency by using unstable resonators.

\*Corresponding author: [f.capolino@uci.edu](mailto:f.capolino@uci.edu)

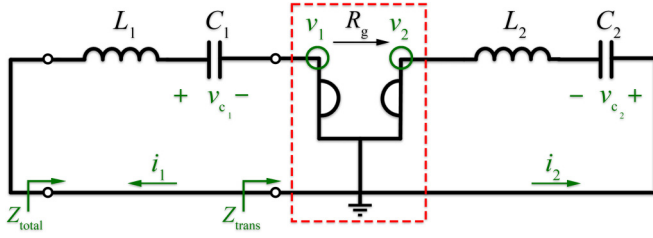


FIG. 1. The schematic illustration of the proposed gyator-based circuit with the ideal gyator is indicated by the red dashed box. In this circuit, two different (unstable) LC resonators are embedded in a series configuration, coupled via an ideal gyator.

In other words, we study the case of two unstable resonators coupled via an ideal gyator. A general mathematical approach for constructing lossless circuits for any conceivable Jordan structure has been developed in Ref. [35], including the simplest possible circuit as in Fig. 1 and other circuits related to the Jordan blocks of higher dimensions. In addition, important issues related to operational stability, perturbation analysis, and sensitivity analysis are studied in Ref. [36], whereas analysis of stability or instability by adding losses to the circuit is not discussed. We show that the gyator-based circuit can achieve an EPD with real eigenfrequency even when two unstable resonators are used in the circuit. Hence, dispersion diagrams corresponding to perturbations in the circuit's parameters show the eigenfrequencies split. Then, we show examples for different cases and analyze the voltage signals by using time-domain simulations. We study the impact of small losses in the circuit and explain how they can make it unstable. Besides, we look at the sensitivity of circuit eigenfrequencies to component variations, and we show that the Puiseux fractional power series expansion well approximates the bifurcation of the eigenfrequency diagram near the EPD [3]. The sensitivity enhancement is attributed to the second root topology of the eigenvalues in parameter space, peculiar to the second-order EPD. Lastly, we examine the gyator-based circuit's enhanced sensitivity and provide a practical scenario to detect physical parameter variations and material characteristics changes. This work is important for understanding the instability in the coupled resonators circuit, in addition to exploring EPD physics in gyator-based circuits. The given analysis and circuit show promising potential in ultrahigh-sensitive sensing applications.

## II. GYRATOR CHARACTERISTIC

A gyator is a two-port component that couples an input port to an output port by a gyration resistance value. It is a lossless and storageless two-port network that converts circuits at the gyator output into their duals, with respect to the gyration resistance value [37]. For instance, this component can make a capacitive circuit behave inductively, a series LC resonator behave like a parallel LC resonator, and so on. This device allows network realizations of two-port devices, which cannot be realized by just the basic components, i.e., resistors, inductors, capacitors, and transformers. In addition, the gyator could be considered a more fundamental circuit component than the ideal transformer because an ideal transformer

can be made by cascading two ideal gyrators, but a gyator cannot be made from transformers [27]. The circuit symbol for the ideal gyator is represented in Fig. 1 (red dashed box), and the defining equations are [27,38]

$$v_2 = R_g i_1, \quad v_1 = -R_g i_2, \quad (1)$$

where  $R_g$  is called gyration resistance and has a unit of ohm. A gyator is a nonreciprocal two-port network represented by an asymmetric impedance matrix  $\underline{\mathbf{Z}}$  as [38]

$$\underline{\mathbf{Z}} = \begin{bmatrix} 0 & -R_g \\ R_g & 0 \end{bmatrix}. \quad (2)$$

## III. EPD CONDITION IN THE LOSSLESS GYRATOR-BASED CIRCUIT

This section provides an analysis of a gyator-based circuit in which two series LC resonators are coupled via an ideal gyator as illustrated in Fig. 1. In the first step, we consider the circuit's components to be lossless. The circuit resembles the one in Ref. [34], but here the two resonance angular frequencies  $\omega_{01} = 1/\sqrt{C_1 L_1}$  and  $\omega_{02} = 1/\sqrt{C_2 L_2}$  of the two uncoupled resonators are imaginary with a negative sign (also the counterpart with the positive sign is a resonance), since we consider three cases: (i) both  $L_1$  and  $L_2$  are negative while the capacitors have positive values, (ii) both  $C_1$  and  $C_2$  are negative while the inductors have positive values, and (iii)  $L_1(C_1)$  and  $C_2(L_2)$  are negative while other elements have positive values. Then, we investigate the conditions for an EPD to occur in the three cases just mentioned. In realistic sensing devices, various sensor types are used. For instance, capacitive sensors are used to sense humidity, temperature, and distance. Proximity sensors and distance measurement sensors are available on the market, which operate based on electromagnetic induction, and the variation of inductance mutual coupling. Some other sensors are based on a perturbation of the inductance. Therefore, both the inductance and the capacitance can be used as sensing components, and we investigate both cases in two separate subsections.

In the past years, EPDs have been found by using balanced loss and gain in a PT-symmetry scheme [13,15,39]. More recently, EPDs have also been found in systems with time-periodic modulation [40,41]. Here, we obtain EPDs by using a negative inductance and a negative capacitance in the gyator-based circuit, constituting an alternative class of EPD-based circuits.

We consider the Kirchhoff voltage law equations in the time domain for two loops of the circuit in Fig. 1. In order to find the solution of the circuit differential equations, it is convenient to define the state vector as  $\Psi(t) \equiv [Q_1, Q_2, \dot{Q}_1, \dot{Q}_2]^T$ , where T denotes the transpose operator. The state vector consists of stored charges in the capacitors  $Q_n = \int i_n dt = C_n v_{c_n}$ , and their time derivative (currents)  $\dot{Q}_n = i_n$ ,  $n = 1$  and 2. We utilize the Liouvillian formalism for this circuit as [34]

$$\frac{d\Psi(t)}{dt} = \underline{\mathbf{M}}\Psi(t), \quad \underline{\mathbf{M}} = \begin{pmatrix} 0 & 0 & 1 & 0 \\ 0 & 0 & 0 & 1 \\ -\omega_{01}^2 & 0 & 0 & \frac{R_g}{L_1} \\ 0 & -\omega_{02}^2 & -\frac{R_g}{L_2} & 0 \end{pmatrix}, \quad (3)$$

where  $\mathbf{M}$  is the  $4 \times 4$  circuit matrix. Assuming time harmonic dependence of the form  $Q_n \propto e^{j\omega t}$ , we obtain the characteristic equation allowing us to find the eigenfrequencies by solving  $\det(\mathbf{M} - j\omega\mathbf{I}) = 0$ , where  $\mathbf{I}$  is the identity matrix. The corresponding characteristic equation of the circuit is

$$\omega^4 - \omega^2 \left( \omega_{01}^2 + \omega_{02}^2 + \frac{R_g^2}{L_1 L_2} \right) + \omega_{01}^2 \omega_{02}^2 = 0, \quad (4)$$

where any solution  $\omega$  is an eigenfrequency of the circuit. In the case of  $R_g = 0$ , the two resonators are uncoupled, and the circuit has two eigenfrequency pairs of  $\omega_{1,3} = \pm\omega_{01}$  and  $\omega_{2,4} = \pm\omega_{02}$  that are purely imaginary (in contrast to the case studied in Ref. [34], where the resonance frequencies have real values). All the  $\omega$  coefficients of the characteristic equation are real, so  $\omega$  and  $\omega^*$  are both roots of the characteristic equation, where  $*$  indicates the complex conjugate operator. Moreover, it is a quadratic equation in  $\omega^2$ ; therefore,  $\omega$  and  $-\omega$  are both solutions of Eq. (4). As we mentioned before, we only consider unstable resonators, i.e., resonators with an imaginary resonance frequency. Therefore, only one circuit element in each resonator should have a negative value, leading to  $\omega_{01}^2$  and  $\omega_{02}^2$  with negative values. After finding the solutions of the characteristic equation, the angular eigenfrequencies (resonance frequencies) of the circuit are expressed as

$$\omega_{1,3} = \pm\sqrt{a+b}, \quad \omega_{2,4} = \pm\sqrt{a-b}, \quad (5)$$

where

$$a = \frac{1}{2}(\omega_{01}^2 + \omega_{02}^2 + \omega_g^2), \quad (6)$$

$$b^2 = a^2 - \omega_{01}^2 \omega_{02}^2, \quad (7)$$

where it has been convenient to define  $\omega_g^2 = R_g^2/(L_1 L_2)$ , which may be positive or negative depending on the considered case. According to Eq. (5), the EPD condition requires

$$b = 0, \quad (8)$$

leading to an EPD angular frequency  $\omega_e = \sqrt{a}$  (with its negative pair  $-\omega_e$ ). According to Eq. (7), the EPD condition is rewritten as  $a^2 = \omega_{01}^2 \omega_{02}^2$ . As in Ref. [34], we consider positive values for  $a$  to have a real EPD angular frequency  $\omega_e$ , so we have

$$\omega_{01}^2 + \omega_{02}^2 + \omega_g^2 > 0. \quad (9)$$

Finally, the EPD frequency is calculated by using Eqs. (6), (7), and (8) as

$$\omega_e = \sqrt{\frac{1}{2}(\omega_{01}^2 + \omega_{02}^2 + \omega_g^2)}. \quad (10)$$

The last equation can also be rewritten as  $\omega_e = \sqrt[4]{\omega_{01}^2 \omega_{02}^2}$ , with the quartic square root defined by taking the positive value; in other words, if we consider that the two unstable frequencies have the following purely imaginary expressions,  $\omega_{01} = -j/\sqrt{|C_1 L_1|}$  and  $\omega_{02} = -j/\sqrt{|C_2 L_2|}$ , the EPD frequency can be expressed as  $\omega_e = \sqrt{-\omega_{01} \omega_{02}}$ . We obtain the desired value of a real EPD frequency by optimizing the values of the components in the circuit. Theoretically, the employed optimization method is not critical, and we need to find the solutions of Eq. (8). Obviously, practical limitations also

affect the selection of suitable constraints for optimization. In the particular case where the two circuits are identical, one has  $\omega_0^2 \equiv \omega_{01}^2 = \omega_{02}^2 = 1/(LC) < 0$ , and the EPD condition reduces to  $4\omega_0^2 = -\omega_g^2$ , which in turns leads to the EPD angular frequency  $\omega_e = \sqrt{-\omega_0^2}$ . In the following subsections, we analyze the circuit in three different cases, i.e., the three different assumptions mentioned earlier.

### A. Negative inductances $L_1$ and $L_2$

As a first case, we consider a negative value for both inductances and a positive value for both capacitances; hence, in this case  $\omega_g^2 > 0$ . According to the required condition for EPD expressed in Eq. (8) and by using Eq. (7), the first and second terms in Eq. (6) are negative and the third term is positive. Equation (10) shows that, if  $|\omega_{01}^2 + \omega_{02}^2| < \omega_g^2$ , we obtain a real value for EPD frequency, and if  $|\omega_{01}^2 + \omega_{02}^2| > \omega_g^2$ , the EPD frequency yields an imaginary value.

We explain the procedure for obtaining an EPD in this circuit by presenting an example. We select  $L_1$ ,  $L_2$ , and  $C_2$  to have standard commercial values. Then, the calculated value for  $C_1$  can be realized by a combination of the standard capacitors values and a trimmer capacitor. Various combinations of values for the circuit's components can satisfy the EPD condition demonstrated in Eq. (8), and here as an example, we consider this set of values:  $L_1 = -47 \mu\text{H}$ ,  $L_2 = -47 \mu\text{H}$ ,  $C_2 = 47 \text{ nF}$ , and  $R_g = 50 \Omega$ . Then, the capacitance of the first resonator is determined by solving the resulting quadratic equation from the EPD condition demonstrated in Eq. (8). In this example, we consider  $C_1$  as a sensing capacitance of the circuit, which has a positive value, and it can detect variations in environmental parameters and transform them into electrical quantities. According to Eq. (8), after solving the quadratic equation, two different values for capacitance in the first resonator are calculated, and we consider  $C_{1,e} = 139.17 \text{ nF}$  for the presented example. In this example, both  $\omega_{01}^2$  and  $\omega_{02}^2$  have negative values, with  $\omega_{01} = -j391 \text{ krad/s}$  and  $\omega_{02} = -j672.82 \text{ krad/s}$ , leading to a positive result for  $a$  in Eq. (6) and real EPD angular frequency  $\omega_e = 512.9 \text{ krad/s}$ . The results in Figs. 2(a), and 2(b) show the real and imaginary parts and the magnitude and phase of perturbed eigenfrequencies obtained from the eigenvalue problem when  $R_g$  of the ideal gyrator is perturbed, revealing the high sensitivity to perturbations. An EPD occurs when both eigenvalues and eigenvectors coalesce. Therefore, the eigenvalues coalesce in both the real and the imaginary parts.

To investigate the time-domain behavior of the circuit under EPD conditions, we use the Keysight Advanced Design System (ADS) circuit simulator. The transient behavior of the coupled resonators with the ideal gyrator is simulated using the time-domain solver with the initial condition  $v_{c_1}(0) = 1 \text{ mV}$ , where  $v_{c_1}(t)$  is the voltage of the capacitor in the left resonator. Figure 2(c) shows the time-domain simulation results of the voltage  $v_1(t)$ , where  $v_1(t)$  is the voltage at the gyrator input port (see Fig. 1). The extracted result is obtained in the time span of 0 to 0.4 ms. The solution of the eigenvalue problem in Eq. (3) and at the EPD is different from any other regular frequency in the dispersion diagram since the system matrix contains repeated eigenvalues associated

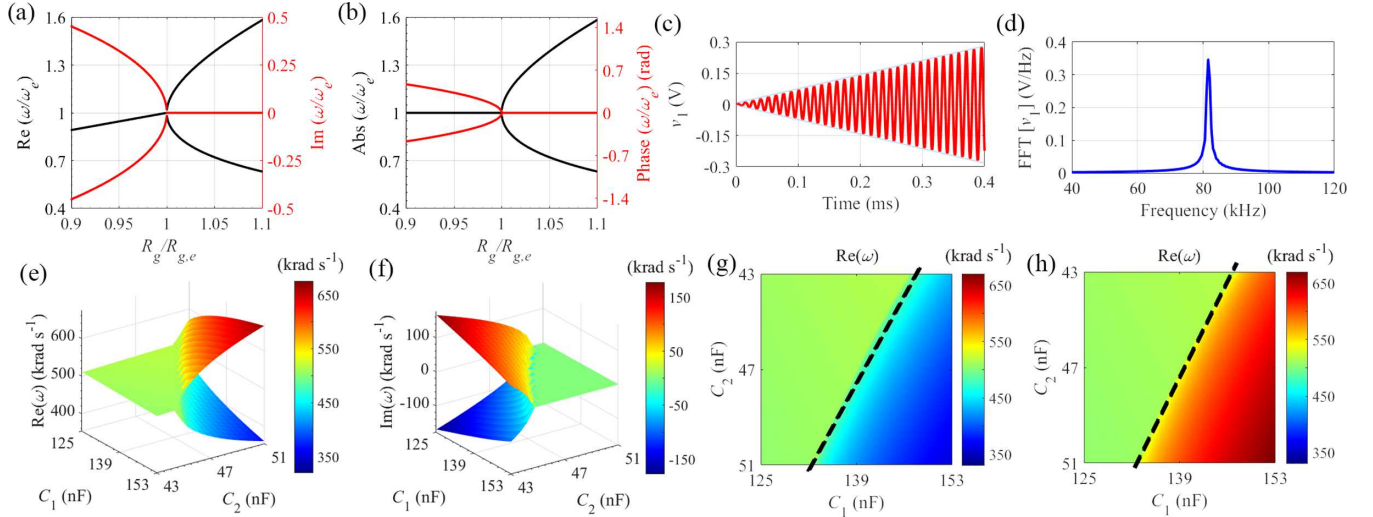


FIG. 2. The sensitivity of the (a) real and imaginary parts and (b) magnitude and phase of the eigenfrequencies to gyration resistance perturbation, while inductances are negative. Voltage  $v_1(t)$  under the EPD condition in the (c) time domain and (d) frequency domain. The frequency-domain result is calculated from 40 to 120 kHz by applying an FFT with  $10^6$  samples in the time window of 0 to 0.4 ms. The three-dimensional plot of the (e) real and (f) imaginary parts of the eigenfrequencies to  $C_1$  and  $C_2$  perturbation. The real part of eigenfrequencies for (g) higher and (h) lower values of resonance frequencies. The colormaps show the resonance frequency values. The black dashed line in these plots shows the EPD.

with one eigenvector. Thus, the time-domain response of the circuit at the second-order EPD is expected to be in the form of  $\Psi(t) \propto t e^{j\omega_e t}$ , as it is shown in Fig. 2(c). The envelope of the voltage signal grows linearly with increasing time, whereas the oscillation frequency is constant. This remarkable feature is peculiar to an EPD, and it is the result of coalescing eigenvalues and eigenvectors that also correspond to a double pole in the circuit (or zero, depending on what is observed). We take a fast Fourier transform (FFT) of the voltage  $v_1(t)$  to show the frequency spectrum, and the calculated result is illustrated in Fig. 2(d). The result is calculated from 40 to 120 kHz by applying an FFT with  $10^6$  samples in the time window of 0 to 0.4 ms. The numerically observed oscillation frequency is  $f_0 = \omega_o/(2\pi) = 81.63$  kHz, which shows the frequency corresponds to the maximum value in Fig. 2(d). The numerically obtained value is in good agreement with the theoretical value calculated above.

So far, we have used the gyrator-based circuit to measure the perturbation near the EPD by varying the gyration resistance. Next, we analyze the circuit's sensitivity to independent perturbations in the positive values of *both* capacitances. We change the capacitance value on each resonator independently and calculate the eigenfrequencies' real and imaginary parts. The three-dimensional result for the calculated eigenfrequencies is illustrated in Figs. 2(e), and 2(f). The elevation value of any point on the surface shows the eigenfrequency, and the associated color helps us to recognize it conveniently. In these figures, only the two solutions with  $\text{Re}(\omega) > 0$  are illustrated. Although the resonance frequency of each resonator in this paper is imaginary, in the specific range of  $C_1$  and  $C_2$ , the EPD frequency is purely real. To utilize these calculated results, the flat version of the three-dimensional diagram for the real part is provided in Figs. 2(g), and 2(h) for higher and lower eigenfrequencies. These figures can help designers in the design procedure to select the proper value for components to

achieve the desired real resonance frequency. The intersection of two surfaces (eigenfrequencies' surface and the surface of the constant  $z$  plane) is a one-dimensional curve. Therefore, there is a different set of values for capacitances to produce oscillation at a certain frequency. Moreover, the intersection of the higher eigenfrequencies' surface and the lower eigenfrequencies' surface indicates the possible EPD that various combinations of capacitances values can yield. Designers can use these figures to pick the proper value in the design steps according to their practical limitations.

### B. Negative capacitances $C_1$ and $C_2$

In the following section, we consider another condition in which negative capacitances are used on both resonators; so  $\omega_g^2 > 0$ . Using the mentioned presumption, the first and second terms in Eq. (6) are negative because of the imaginary value of the resonance frequencies of resonators, and the third term is positive. So, if the EPD condition is met, the sign of  $a$  in Eq. (6) indicates whether the eigenfrequency is real or imaginary. According to Eq. (10), if  $|\omega_{01}^2 + \omega_{02}^2| < \omega_g^2$ , we get a real value for the EPD frequency, and if  $|\omega_{01}^2 + \omega_{02}^2| > \omega_g^2$ , the EPD frequency is imaginary.

Different combinations of values for the circuit's components can satisfy the EPD condition demonstrated in Eq. (8), and here as an example, we use this set of values:  $C_1 = -47$  nF,  $C_2 = -47$  nF,  $L_2 = 47$   $\mu$ H, and  $R_g = 50$   $\Omega$ . The inductance value on the left resonator is calculated by solving the resulting quadratic equation from Eq. (8). In the presented example,  $L_1$  can be a sensing inductor in a system. According to Eq. (8), two different values for inductance in the first resonator are calculated after solving the quadratic equation. We consider  $L_{1,e} = 15.87$   $\mu$ H for this example, so both  $\omega_{01}^2$  and  $\omega_{02}^2$  have negative values, with  $\omega_{01} = -j1.16$  Mrad/s and  $\omega_{02} = -j672.82$  krad/s. Then, we obtain a positive value

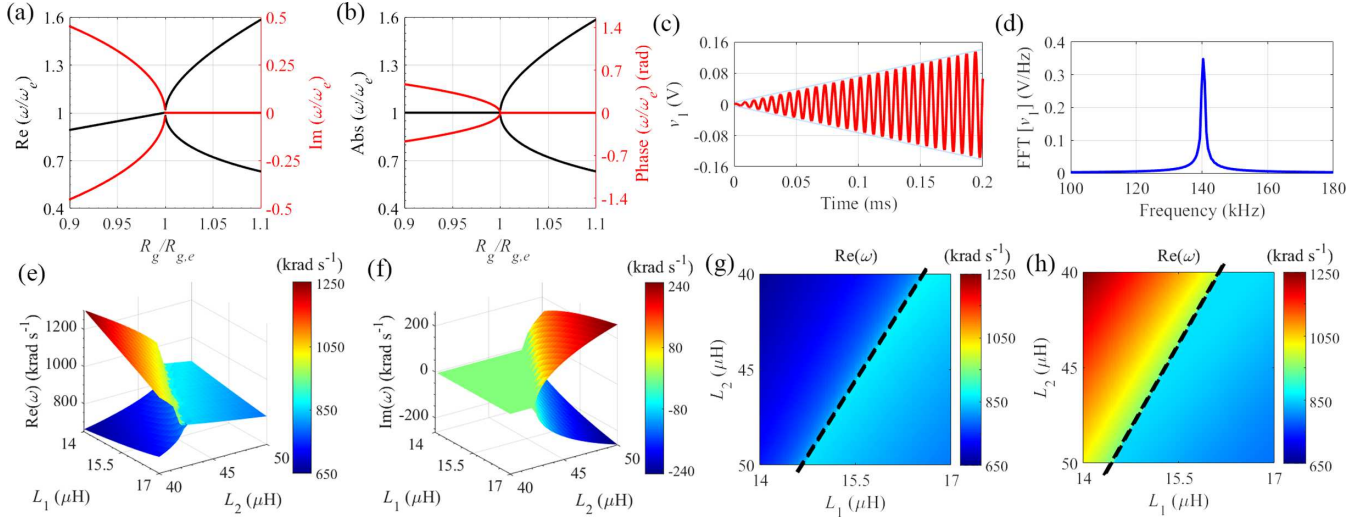


FIG. 3. The sensitivity of the (a) real and imaginary parts and the (b) magnitude and phase of the eigenfrequencies to gyration resistance perturbation, while capacitances are negative. Voltage  $v_1(t)$  under the EPD condition in the (c) time domain and (d) frequency domain. The frequency domain result is calculated from 100 to 180 kHz by applying an FFT with  $10^6$  samples in the time window of 0 to 0.2 ms. The three-dimensional plot of the (e) real and (f) imaginary parts of the eigenfrequencies to  $L_1$  and  $L_2$  perturbation. The real part of eigenfrequencies for (g) higher and (h) lower values of resonance frequencies. The colormaps show the resonance frequency values. The black dashed line in these plots shows the EPD.

for  $a$  in Eq. (6), leading to a real EPD angular frequency of  $\omega_e = 881.6$  krad/s. The results in Figs. 3(a), and 3(b) show the real and imaginary parts and the magnitude and phase of eigenfrequencies obtained by perturbing  $R_g$  near the value that made the EPD.

The time-domain simulation result by using the Keysight ADS with an initial condition  $v_1(0) = 1$  mV is presented in Fig. 3(c). The voltage  $v_1(t)$  is calculated in the time interval of 0 to 0.2 ms. Figure 3(c) shows the envelope of  $v_1(t)$  is growing linearly with increasing time. The growing signal demonstrates that the circuit eigenvalues coalesce, and the output envelope rises linearly at the second-order EPD frequency. In order to evaluate the oscillation frequency from the time-domain simulation, we take an FFT of voltage  $v_1(t)$  from 100 to 180 kHz using  $10^6$  samples in the time window of 0 to 0.2 ms. The calculated spectrum is shown in Fig. 3(d), showing an oscillation frequency of  $f_0 = \omega_o/(2\pi) = 140.31$  kHz, which is in good agreement with the calculated theoretical value obtained from Eq. (10).

In the following step, we investigate the circuit's sensitivity to independent perturbations in the value of both inductances. The real and imaginary parts of the eigenfrequencies are calculated when the values of the inductances are changed. The three-dimensional eigenfrequency map of the two solutions with  $\text{Re}(\omega) > 0$  is shown in Figs. 3(e) and 3(f). In order to provide a better representation, the flat view of the three-dimensional diagram for the real part is shown in Figs. 3(g) and 3(h) for higher and lower eigenfrequencies.

### C. Negative inductance on one side and negative capacitance on the other side

In this last case, different constraints for components value are considered. We assume a component with a negative value

on one side (capacitance or inductance) and the other component with a negative value on the other side (inductance or capacitance); hence, in this case  $\omega_g^2 < 0$ . For instance, we consider a negative inductance on the right resonator and a negative capacitance on the left resonator. So, we have two unstable resonators when they are uncoupled. When two resonators are coupled, EPD should satisfy Eq. (8). According to Eq. (10), all terms inside the square root are negative, and the sum of negative values is always negative. As a result, it is impossible to achieve an EPD with a real eigenfrequency under the assumption mentioned above. Since we focus on cases with real EPD frequency in this paper, we skip considering this condition in the rest of the paper.

## IV. FREQUENCY-DOMAIN ANALYSIS OF THE RESONANCES IN a LOSSLESS GYRATOR-BASED CIRCUIT

We demonstrate how the EPD regime is associated with a special kind of circuit's resonance, directly observed in frequency-domain circuit analysis. First, we calculate the transferred impedance on the left port of the gyrator in Fig. 1, which is

$$Z_{\text{trans}}(\omega) = \frac{R_g^2}{Z_2(\omega)}, \quad (11)$$

where  $Z_2(\omega) = j\omega L_2 + 1/(j\omega C_2)$  is the impedance of the LC tank on the right side of the gyrator. The total impedance observed from the input port (see Fig. 1) is

$$Z_{\text{total}}(\omega) \triangleq Z_1(\omega) + Z_{\text{trans}}(\omega) = Z_1(\omega) + \frac{R_g^2}{Z_2(\omega)}, \quad (12)$$

where  $Z_1(\omega) = j\omega L_1 + 1/(j\omega C_1)$  is the impedance of the LC tank on the left side of the gyrator. The complex-valued

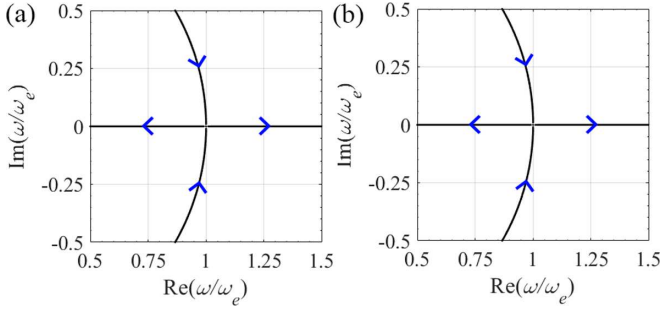


FIG. 4. Root locus of zeros of  $Z_{\text{total}}(\omega) = 0$  shows the real and imaginary parts of the resonance frequencies of the circuit when varying gyration resistance (arrows represent growing  $R_g$  values). In these figures, we consider two cases with a negative value of (a) both inductances and (b) both capacitances, discussed in Sec. III. At the EPD, the system's total impedance is  $Z_{\text{total}}(\omega) \propto (\omega - \omega_e)^2$ ; hence, it exhibits a double zero at  $\omega_e$ .

resonance frequencies of the circuit are calculated by imposing  $Z_{\text{total}}(\omega) = 0$ . Figure 4 shows the zeros of such total impedance  $Z_{\text{total}}(\omega)$  for various gyration resistance values (arrows represent growing  $R_g$  values). When considering the EPD gyration resistance  $R_g = R_{g,e} = 50 \Omega$ , one has  $Z_{\text{total}}(\omega) \propto (\omega - \omega_e)^2$ ; i.e., the two zeros coincide with the EPD angular frequency  $\omega_e$ , which is also the point where the two curves in Fig. 4 meet. For gyration resistances  $R_g < R_{g,e}$ , the two resonance angular frequencies are complex conjugate, consistent with the result in Fig. 4. Also, for gyration resistances such that  $R_g > R_{g,e}$ , the two resonance angular frequencies are purely real. In other words, the EPD frequency coincides with the double zeros of the frequency spectrum, or double poles, depending on the way the circuit is described.

## V. EPD IN THE LOSSY GYRATOR-BASED CIRCUIT

The following section analyzes the EPD condition in the gyration-based circuit by accounting for series resistors  $R_1$  and  $R_2$  in resonators as illustrated in Fig. 5. A procedure analogous to the one discussed earlier, using the same state vector  $\Psi \equiv [Q_1, Q_2, \dot{Q}_1, \dot{Q}_2]^T$ , leads to [34]

$$\frac{d\Psi}{dt} = \mathbf{M}\Psi, \quad \mathbf{M} = \begin{pmatrix} 0 & 0 & 1 & 0 \\ 0 & 0 & 0 & 1 \\ -\omega_{01}^2 & 0 & -\gamma_1 & \frac{R_g}{L_1} \\ 0 & -\omega_{02}^2 & -\frac{R_g}{L_2} & -\gamma_2 \end{pmatrix}. \quad (13)$$

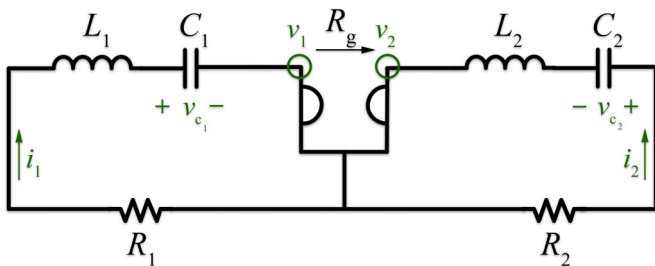


FIG. 5. Schematic view of the lossy gyration-based circuit, with a resistor in each resonator.

In the presented lossy circuit matrix,  $\gamma_1 = R_1/L_1$  and  $\gamma_2 = R_2/L_2$  determine losses in each resonator. The eigenfrequencies of the circuit are calculated by solving the following characteristic equation,

$$\omega^4 - j\omega^3(\gamma_1 - \gamma_2) - \omega^2 \left( \omega_{01}^2 + \omega_{02}^2 + \gamma_1\gamma_2 + \frac{R_g^2}{L_1L_2} \right) + j\omega(\gamma_1\omega_{02}^2 + \gamma_2\omega_{01}^2) + \omega_{01}^2\omega_{02}^2 = 0. \quad (14)$$

The coefficients of the odd-power terms of the angular eigenfrequency in the characteristic equation are imaginary; therefore,  $\omega$  and  $-\omega^*$  are both roots of the characteristic equation. In order to obtain a stable circuit with real-valued eigenfrequencies, the coefficients of the odd-power terms in the characteristic equation of Eq. (14),  $-j(\gamma_1 - \gamma_2)$  and  $j(\gamma_1\omega_{02}^2 + \gamma_2\omega_{01}^2)$ , should vanish, otherwise a complex eigenfrequency is needed to satisfy the characteristic equation. The coefficient of the  $\omega^3$  term is zero when  $\gamma_1 = \gamma_2$ , but according to this condition, the coefficient of the  $\omega$  term is nonzero because  $\omega_{01}^2$  and  $\omega_{02}^2$  are both negative. Moreover, the coefficient of the  $\omega$  term never vanishes when both resonators are lossy because both  $\omega_{01}^2$  and  $\omega_{02}^2$  have the same sign. Consequently, it is not possible to have all real-valued coefficients in the characteristic polynomials, except when  $\gamma_1 = \gamma_2 = 0$ , which corresponds to a lossless circuit.

### A. RLC resonators with negative inductances $L_1$ and $L_2$

In the first case, we assume inductances with negative values. In Figs. 6(a) and 6(b),  $\gamma_1$  is perturbed while we assume  $\gamma_2 = 0$ , whereas in Figs. 6(c), and 6(d),  $\gamma_2$  is perturbed while  $\gamma_1 = 0$ . These four plots present the real and imaginary parts and the magnitude and phase of eigenfrequencies when the resistances  $R_1$  and  $R_2$  are perturbed individually. We use the same values for the circuit components as already used in the lossless circuit presented in Sec. III A. The normalization term  $\omega_e$  is the EPD angular frequency obtained when  $\gamma_1 = \gamma_2 = 0$ , which is the same EPD frequency as the lossless circuit. In this case, losses in the circuit are represented by negative  $\gamma_1$  and  $\gamma_2$  since  $L_1$ , and  $L_2$  are negative, so the right side of the figure axes show the loss and the left side of the axes represent the gain in the circuit through a negative resistance. In Figs. 6(a)–6(d), we recognize the bifurcations of the real and imaginary parts and the magnitude and phase of the eigenfrequencies, so the circuit is extremely sensitive to variations of resistances in the vicinity of EPD. By perturbing  $\gamma_1$  or  $\gamma_2$  away from  $\gamma_1 = \gamma_2 = 0$ , the circuit becomes unstable, and it begins to self-oscillate at a frequency associated with the real part of the unstable angular eigenfrequency. In addition, we show the real and imaginary parts of the eigenfrequencies by separately perturbing the resistances on both sides in Figs. 6(e) and 6(f). The black contour curves in these three-dimensional figures show constant real or imaginary parts of the eigenfrequencies. We observe that by adding either loss or gain, the circuit becomes unstable. Instability in the circuit is not due to the instability of the uncoupled resonators, but rather it is unstable because of the addition of losses, as was the case in Ref. [34] for different configurations. When  $\gamma_1$  or  $\gamma_2$  is perturbed from the EPD, the oscillation frequency is shifted from the EPD frequency, and it could be measured

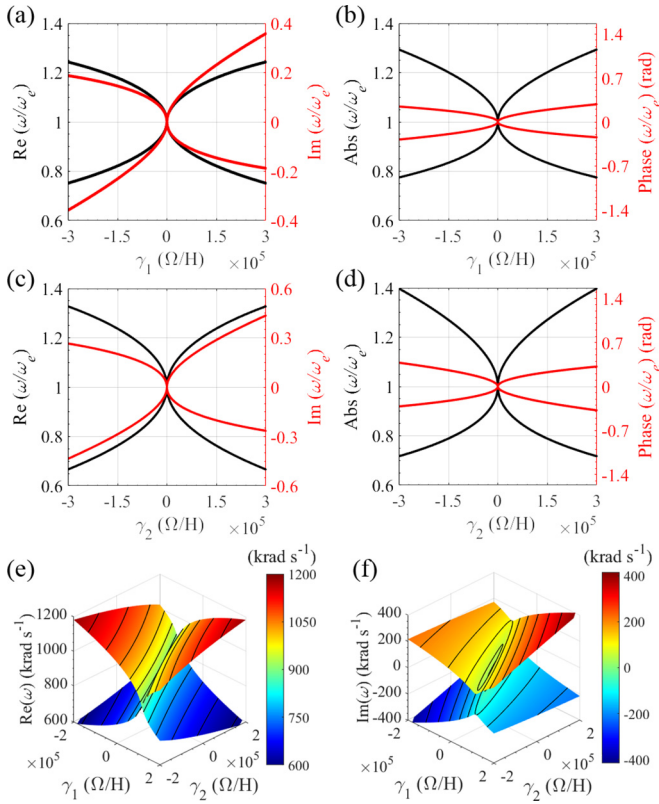


FIG. 6. Case with negative value of the inductances on both resonators. Variation of (a) real and imaginary parts and (b) magnitude and phase of the angular eigenfrequencies to a resistor perturbation on the left resonator, i.e., when  $-\gamma_1$  changes and  $\gamma_2 = 0$ . (c) and (d) Same as in panels (a) and (b), but the resistor perturbation is on the right resonator, i.e.,  $-\gamma_2$  changes and  $\gamma_1 = 0$ . Variation of (e) real and (f) imaginary parts of the angular eigenfrequencies to independent resistor perturbation on both sides.

for sensing applications. The eigenfrequency with a negative imaginary part is associated with an exponentially growing signal (instability). Considering the existence of instability, there are a few possible ways of operation: preventing the system from reaching saturation by switching off the circuit, partially compensating for losses, or making the circuit an oscillator. In the partial compensation scheme, the instability effect due to losses in the circuit can be counterbalanced by adding an independent series gain to each resonator. A negative resistance can be easily implemented using the same opamp-based circuit designed to achieve negative inductance and capacitance. This issue is beyond the scope of this paper, and it seems a complicated strategy for stability. We believe that exploiting the system's instability may be an excellent strategy to design sensitive oscillators that work as sensors; this could be the subject of future investigations.

### B. RLC resonators with negative capacitances $C_1$ and $C_2$

In the second case, we consider the negative value for capacitances. In Figs. 7(a) and 7(b),  $\gamma_1$  is perturbed while we consider  $\gamma_2 = 0$ , and in Figs. 7(c), and 7(d),  $\gamma_2$  is perturbed

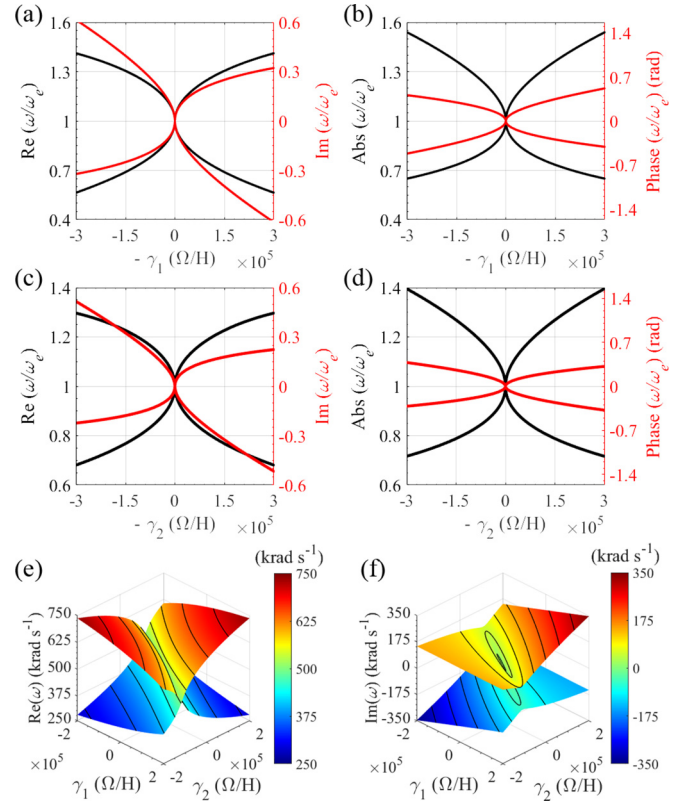


FIG. 7. Case with negative value of the capacitances on both resonators. Variation of (a) real and imaginary parts and (b) magnitude and phase of the angular eigenfrequencies to a resistor perturbation on the left resonator, i.e., when  $-\gamma_1$  changes and  $\gamma_2 = 0$ . (c) and (d) Same as in panels (a) and (b), but the resistor perturbation is on the right resonator, i.e.,  $-\gamma_2$  changes and  $\gamma_1 = 0$ . Variation of (e) real and (f) imaginary parts of the angular eigenfrequencies to independent resistor perturbation on both sides.

while  $\gamma_1 = 0$ . These figures show the real and imaginary parts of the eigenfrequencies when each resistor is perturbed individually. We use the same values for the circuit components as used earlier in the lossless circuit shown in Sec. III B, and the EPD angular frequency is obtained for these circuit parameters when  $\gamma_1 = \gamma_2 = 0$ , which is the same EPD frequency as the lossless circuit. In Figs. 7(a)–7(d), we observe the bifurcations of the real and imaginary parts and the magnitude and phase of the eigenfrequencies, so the circuit exhibits extreme sensitivity to resistance value variations in the vicinity of EPD. We show the real and imaginary parts of the eigenfrequencies by independently changing the resistances on both sides in Figs. 7(e) and 7(f). The black contour curves in these three-dimensional figures show constant real or imaginary parts of the eigenfrequencies. Angular eigenfrequencies are complex valued when perturbing  $\gamma_1$  and  $\gamma_2$  away from  $\gamma_1 = \gamma_2 = 0$ ; hence, the circuit gets unstable and it starts to oscillate at a fundamental frequency associated with the real part of the unstable angular eigenfrequency. In Figs. 7(a)–7(f), both conditions  $\gamma_1 > 0$  and  $\gamma_2 > 0$  represent loss, whereas the conditions  $\gamma_1 < 0$  and  $\gamma_2 < 0$  represent gain in the circuit through a negative resistance.

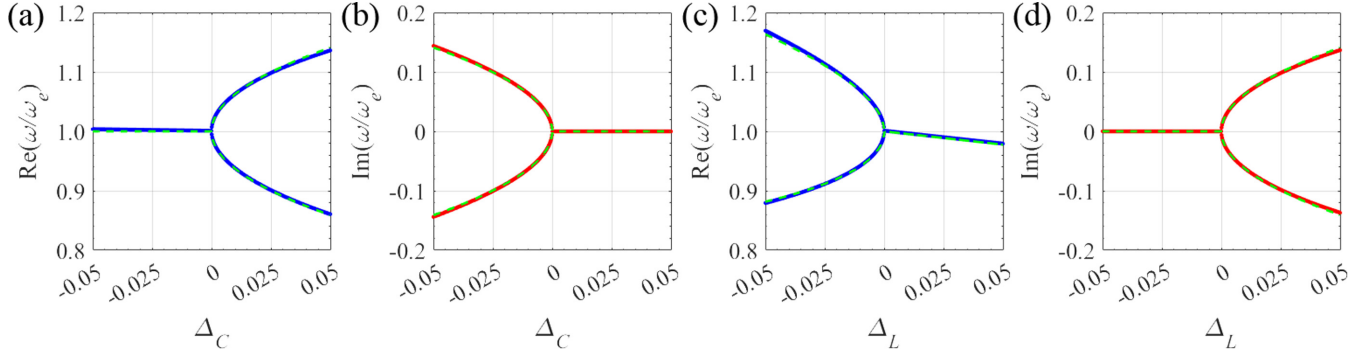


FIG. 8. Sensitivity of (a) real and (b) imaginary parts of the eigenfrequencies to a capacitance perturbation (solid lines),  $\Delta_C = (C_1 - C_{1,e})/C_{1,e}$ , while the inductance values on both sides are negative. Dashed lines show the perturbed eigenfrequencies according to the Puiseux expansion up to its first order. Sensitivity of (c) real and (d) imaginary parts of the eigenfrequencies to an inductance perturbation (solid lines),  $\Delta_L = (L_1 - L_{1,e})/L_{1,e}$ , while the capacitance values on both sides are negative. Dashed lines show the perturbed eigenfrequencies according to the Puiseux expansion up to its second order.

## VI. HIGH-SENSITIVITY AND PUISEUX FRACTIONAL POWER SERIES EXPANSION

Eigenfrequencies at EPDs are extremely sensitive to perturbations of the circuit elements, a property that is peculiar to the EPD condition. We study the circuit under EPD perturbation to investigate the circuit's sensitivity near the EPD. We demonstrate how small perturbations in a component's value perturb the eigenfrequencies of the circuit. In order to do this analysis, the relative circuit perturbation  $\Delta_X$  is defined as

$$\Delta_X = \frac{X - X_e}{X_e}, \quad (15)$$

where  $X$  is the perturbed parameter value, and  $X_e$  is its unperturbed value that provides the EPD. The perturbation in  $\Delta_X$  value leads to a perturbed circuit matrix  $\mathbf{M}(\Delta_X)$ . We demonstrate the extreme sensitivity to extrinsic perturbation by resorting to the general theory of EPD and utilizing the Puiseux fractional power series expansion [3]. Accordingly, when a small relative perturbation in the component value  $\Delta_X$  is applied, the resulting two different eigenfrequencies  $\omega_p(\Delta_X)$ , with  $p = 1$  and  $2$ , are estimated using the convergent Puiseux series. Here we provide the first two terms to estimate the eigenfrequencies near an EPD, using the explicit formulas given in Ref. [42]:

$$\omega_p(\Delta_X) \approx \omega_e + (-1)^p \alpha_1 \sqrt{\Delta_X} + \alpha_2 \Delta_X, \quad (16)$$

$$\alpha_1 = \sqrt{-\frac{\frac{\partial H(\Delta_X, \omega)}{\partial \Delta_X}}{\frac{1}{2!} \frac{\partial^2 H(\Delta_X, \omega)}{\partial \omega^2}}}\bigg|_{\Delta_X=0, \omega=\omega_e}, \quad (17)$$

$$\alpha_2 = -\frac{\alpha_1^2 \frac{1}{3!} \frac{\partial^3 H(\Delta_X, \omega)}{\partial \omega^3} + \frac{\partial^2 H(\Delta_X, \omega)}{\partial \omega \partial \Delta_X}}{\frac{\partial^2 H(\Delta_X, \omega)}{\partial \omega^2}}\bigg|_{\Delta_X=0, \omega=\omega_e}, \quad (18)$$

where  $H(\Delta_X, \omega) = \det[\mathbf{M}(\Delta_X) - j\omega\mathbf{I}]$ , and  $\alpha_1$  and  $\alpha_2$  are first- and second-order coefficients, respectively. Equation (16) indicates that for a tiny perturbation in component value  $\Delta_X \ll 1$  the eigenvalues change sharply from their original degenerate value due to the square

root function, which is an essential characteristic of second-order EPDs.

Typically, the inductor or capacitor changes in response to an external perturbation of the parameter of interest, leading to a shift in resonance frequency. We consider variations of  $L_1$ , or  $C_1$ , one at the time, and the calculated real and imaginary parts of the eigenfrequencies near the EPD are shown in Fig. 8. In the first case, the perturbation parameter is the capacitance,  $\Delta_C = (C_1 - C_{1,e})/C_{1,e}$ , and a negative value for both inductances is assumed, so the first-order Puiseux expansion coefficient is calculated as  $\alpha_1 = 3.228 \times 10^5$  rad/s. To calculate the coefficients, we use the components value utilized in Sec. III A. Figures 8(a) and 8(b) exhibit the real and imaginary parts of the perturbed eigenfrequencies  $\omega$  obtained from the eigenvalue problem after perturbing  $\Delta_C$ . Furthermore, green dashed lines in these figures demonstrate that such perturbed eigenfrequencies are well estimated with high accuracy by using the Puiseux expansion truncated at its first order. For a negative but small value of  $\Delta_C$ , the imaginary part of the eigenfrequencies experiences a rapid change, and its real part remains constant. On the other hand, a very small positive value of  $\Delta_C$  causes a sharp change in the real part of the eigenfrequencies while its imaginary part remains unchanged.

In the second example, the inductance value in the left resonator is considered as a perturbed parameter,  $\Delta_L = (L_1 - L_{1,e})/L_{1,e}$ , whereas the capacitance values are both negative. By using Eqs. (17) and (18) and using the components values utilized in Sec. III B, the coefficients of the Puiseux expansion are calculated as  $\alpha_1 = j5.548 \times 10^5$  rad/s and  $\alpha_2 = -3.960 \times 10^5$  rad/s. The calculated results in Figs. 8(c) and 8(d) show the two branches (solid lines) of the exact perturbed eigenfrequencies evaluated from the eigenvalue problem when the external perturbation is applied to the circuit. These two plots show that the perturbed eigenfrequencies are estimated accurately by applying the Puiseux expansion truncated at its second order (dashed lines). For a tiny value of positive perturbation, the imaginary part of the eigenfrequencies undergoes sharp changes, while its real part remains approximately unchanged. However, a small negative



perturbation in the inductance value rapidly changes the real part of the two eigenfrequencies away from the EPD eigenfrequency. The bifurcation in the diagram, described by a square root, is the most exceptional physical property associated with the EPD. It can be employed to devise ultrasensitive sensors for various applications [16,43–45].

## VII. SENSING SCENARIO FOR LIQUID CONTENT MEASUREMENT

In recent years various well-established techniques have been proposed to measure the liquid level, such as light-reflection sensors [46], chirped fiber Bragg grating [47,48], fiber optic sensors [49–51], ultrasonic Lamb waves [52], and capacitive sensors [53–56]. The use of a capacitive sensor is a well-known method for liquid level measurement [57]. This kind of sensor has been proven to be stable, can be assembled using various materials, and can provide high resolution [58]. The principle of operation of capacitive sensors is that they convert a variation in position, or material characteristics, into measurable electrical signals [59]. Capacitive sensors are operated by changing any of the three main parameters: relative dielectric constant, area of capacitive plates, and distance between the plates. In conventional methods, a capacitive liquid level detector can sense the fluid level by measuring variations in capacitance made between two conducting plates embedded outside a nonconducting tank or immersed in the liquid [57,60]. The same concept applies when the liquid occupies a varying volume percentage of a mixture's components.

In order to compare the advantages of the EPD-based sensors with conventional sensors based on a single LC circuit, we use a simple ideal scheme for liquid content measurement. We demonstrate that the sensitivity of a gyrator-based circuit by operating near the EPD is much higher than the sensitivity of a conventional LC resonator circuit. We provide the required setup and the measurement procedure to measure the liquid volume. Here, we use the following set of values for the components in the gyrator-based circuit:  $L_1 = -4.7$  nH,  $L_2 = -4.7$  nH,  $C_2 = 47$  pF, and  $R_g = 50$   $\Omega$ . Consider a cylindrical glass with top and bottom metal plates. This structure can serve as a variable capacitor in which the volume of filled liquid (or a percentage of a mixture) can change the total capacitance. A schematic structure for this scenario is illustrated in Fig. 9(a). The designed device includes the gyrator-based circuit (see Fig. 1) where the positive capacitor on the left side is the cylindrical container with height  $d_2 = 3.0142$  cm, of which a height  $d_1$  is filled with water, and the area of metal plate is  $A = 100$  cm<sup>2</sup>. Pure water is assumed to have a relative permittivity of  $\epsilon_r = 78.7$  at  $T = 22.0$  °C, and we neglect losses in this simple case [61]. Two series variable capacitors model the structure in which the bottom one has a capacitance of  $C_{\text{filled}} = \epsilon_0 \epsilon_r A / d_1$  and the top one has a capacitance of  $C_{\text{empty}} = \epsilon_0 A / (d_2 - d_1)$ . The total capacitance is  $C_{\text{total}} = C_{\text{filled}} C_{\text{empty}} / (C_{\text{filled}} + C_{\text{empty}})$ , which changes when varying the water level. By opening the top inlet, the height of the water will increase, so the capacitance value will be increased. On the contrary, the water's height decreases when opening the bottom outlet, and the total capacitance value will be decreased. In summary, the level of water is related to the capacitance, and the perturbation in the value

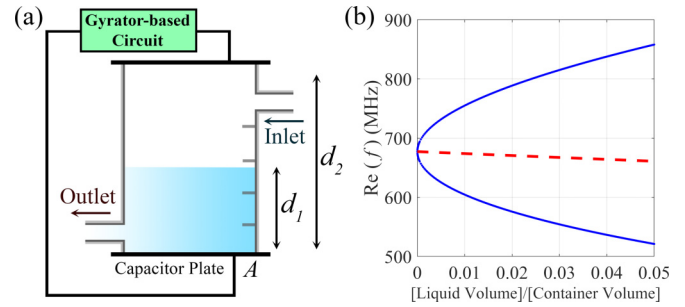


FIG. 9. (a) Schematic illustration of a device for liquid level measurement. (b) The EPD is designed at a given level of water content (0 in the figure). The solid blue line in the plot shows the two resonance frequencies of the gyrator-based circuit versus water level variation with very high sensitivity near 0. The red dashed line shows the resonance frequency of a single resonator when the water content changes. The EPD-based circuit and the single LC resonator have the same resonance frequency at 0. It is clear that the EPD-based circuit provides much higher sensitivity to the capacitance perturbation than the single LC resonator.

of capacitance will change a circuit's eigenfrequencies. Using the steps explained in Sec. III and by solving the eigenvalue problem, the plot of resonance frequency versus water level percentage for this specific example is illustrated in Fig. 9(b) by the solid blue line. The measuring scheme is very sensitive near 0 water content. The EPD can be designed for different water contents, so the frequency variation caused by changes in the water level around that mentioned level will be very sensitive. We now compare the sensitivity of the EPD-based scheme with that of a single LC resonator. We consider an LC resonator with the resonance frequency of  $\omega_0 = \omega_e$ , i.e., coincident with one of the EPD systems. We assume that the sensing capacitor is the same as the one in Fig. 9, i.e., the same as that considered in the EPD system. The variation in the resonance frequency by perturbing the capacitance as described above, i.e., the level of water content, is shown in Fig. 9(b) by the red dashed line. It is clear that the EPD-based bifurcation in the dispersion diagram, characterized by a square root, dramatically enhances the circuit's sensitivity compared to the sensitivity of the single LC resonator to the same capacitance perturbation.

In the proposed scheme for liquid content measurement, we assume that the gyrator-based circuit works in the stable region where eigenfrequencies are purely real. However, when considering the instabilities generated by losses, one eigenfrequency has a negative imaginary value, as explained in Sec. V. Consequently, the circuit starts having growing oscillations. The exponential growth rate can be controlled in two ways: either by stopping (switching off) the circuit to reach saturation or by letting it saturate. In this latter case, the gyrator-based circuit should be designed as a sensor that oscillates. The circuit can be used to sense physical or chemical parameters changes by measuring the oscillation frequency variations.

## VIII. CONCLUSIONS

A second-order EPD with a real (degenerate) eigenfrequency in a gyrator-based circuit is achieved using two

unstable series LC resonators coupled via a gyrator. Each unstable resonator has either a negative capacitance or a negative inductance; hence, the resonance frequency of each resonator is purely imaginary when they are uncoupled. We have demonstrated that coupling the two unstable resonators can make the overall circuit marginally stable with a purely real-valued EPD frequency. We have also shown that the system becomes unstable when small losses or gains are considered in the circuit. We investigated and demonstrated the enhanced sensitivity to perturbations when operating at the EPD. In particular, we have considered the perturbation of the gyration resistance, capacitance, and inductance. The perturbation in physical or chemical parameters affects the circuit component's value in realistic applications. Such a perturbation

could be estimated by measuring the shift of resonance frequencies that follow the square-root behavior typical of an EPD perturbation. The presented results may impact sensing technology, security systems, particle monitoring, and motion sensors. In addition, future studies using resonators with purely imaginary frequencies like waveguides below cutoff may help miniaturize microwave sensing devices.

#### ACKNOWLEDGMENTS

This material is based upon work supported by the National Science Foundation (NSF) under Grant No. ECCS-1711975 and by Air Force Office of Scientific Research (AFOSR) Grant No. FA9550-19-1-0103.

- 
- [1] M. I. Vishik and L. A. Lyusternik, The solution of some perturbation problems for matrices and selfadjoint or non-selfadjoint differential equations I, *Russ. Math. Surv.* **15**, 1 (1960).
- [2] P. Lancaster, On eigenvalues of matrices dependent on a parameter, *Numer. Math.* **6**, 377 (1964).
- [3] T. Kato, *Perturbation Theory for Linear Operators*, 1st ed. (Springer-Verlag, New York, 1966).
- [4] A. P. Seyranian, Sensitivity analysis of multiple eigenvalues, *J. Struct. Mech.* **21**, 261 (1993).
- [5] W. Heiss, Repulsion of resonance states and exceptional points, *Phys. Rev. E* **61**, 929 (2000).
- [6] A. Figotin and I. Vitebskiy, Oblique frozen modes in periodic layered media, *Phys. Rev. E* **68**, 036609 (2003).
- [7] W. Heiss, Exceptional points—Their universal occurrence and their physical significance, *Czech. J. Phys.* **54**, 1091 (2004).
- [8] A. Figotin and I. Vitebskiy, Gigantic transmission band-edge resonance in periodic stacks of anisotropic layers, *Phys. Rev. E* **72**, 036619 (2005).
- [9] H. Ramezani, T. Kottos, V. Kovanis, and D. N. Christodoulides, Exceptional-point dynamics in photonic honeycomb lattices with  $\mathcal{PT}$  symmetry, *Phys. Rev. A* **85**, 013818 (2012).
- [10] M. V. Berry, Physics of nonhermitian degeneracies, *Czech. J. Phys.* **54**, 1039 (2004).
- [11] C. M. Bender and S. Boettcher, Real Spectra in Non-Hermitian Hamiltonians Having  $\mathcal{PT}$  Symmetry, *Phys. Rev. Lett.* **80**, 5243 (1998).
- [12] H. Hodaei, M.-A. Miri, M. Heinrich, D. N. Christodoulides, and M. Khajavikhan, Parity-time symmetric microring lasers, *Science* **346**, 975 (2014).
- [13] P.-Y. Chen, M. Sakhdari, M. Hajizadegan, Q. Cui, M. M.-C. Cheng, R. El-Ganainy, and A. Alu, Generalized parity-time symmetry condition for enhanced sensor telemetry, *Nat. Electron.* **1**, 297 (2018).
- [14] T. Stehmann, W. Heiss, and F. Scholtz, Observation of exceptional points in electronic circuits, *J. Phys. A: Math. Gen.* **37**, 7813 (2004).
- [15] J. Schindler, A. Li, M. C. Zheng, F. M. Ellis, and T. Kottos, Experimental study of active LRC circuits with  $\mathcal{PT}$  symmetries, *Phys. Rev. A* **84**, 040101(R) (2011).
- [16] M. Sakhdari, M. Hajizadegan, Y. Li, M. M.-C. Cheng, J. C. Hung, and P.-Y. Chen, Ultrasensitive, parity–time–symmetric wireless reactive and resistive sensors, *IEEE Sens. J.* **18**, 9548 (2018).
- [17] Y. J. Zhang, H. Kwon, M.-A. Miri, E. Kallos, H. Cano-Garcia, M. S. Tong, and A. Alu, Noninvasive Glucose Sensor Based on Parity-Time Symmetry, *Phys. Rev. Appl.* **11**, 044049 (2019).
- [18] J. Wiersig, Enhancing the Sensitivity of Frequency and Energy Splitting Detection by Using Exceptional Points: Application to Microcavity Sensors for Single-Particle Detection, *Phys. Rev. Lett.* **112**, 203901 (2014).
- [19] J. Wiersig, Sensors operating at exceptional points: General theory, *Phys. Rev. A* **93**, 033809 (2016).
- [20] J. Wiersig, Robustness of exceptional-point-based sensors against parametric noise: The role of Hamiltonian and Liouvillian degeneracies, *Phys. Rev. A* **101**, 053846 (2020).
- [21] J. Wiersig, Review of exceptional point-based sensors, *Photonics Res.* **8**, 1457 (2020).
- [22] J. Wiersig, Prospects and fundamental limits in exceptional point-based sensing, *Nat. Commun.* **11**, 2454 (2020).
- [23] S. Gwak, H. Kim, H.-H. Yu, J. Ryu, C.-M. Kim, and C.-H. Yi, Rayleigh scatterer-induced steady exceptional points of stable-island modes in a deformed optical microdisk, *Opt. Lett.* **46**, 2980 (2021).
- [24] K. Rouhi, R. Marosi, T. Mealy, A. F. Abdelshafy, A. Figotin, and F. Capolino, Exceptional degeneracies in traveling wave tubes with dispersive slow-wave structure including space-charge effect, *Appl. Phys. Lett.* **118**, 263506 (2021).
- [25] P. Djourje, Y. Pennec, and B. Djafari-Rouhani, Exceptional Point Enhances Sensitivity of Optomechanical Mass Sensors, *Phys. Rev. Appl.* **12**, 024002 (2019).
- [26] Q. Wang and Y. Liu, Review of optical fiber bending/curvature sensor, *Measurement* **130**, 161 (2018).
- [27] B. D. Tellegen, The gyrator, a new electric network element, *Philips Res. Rep.* **3**, 81 (1948).
- [28] D. C. Hamill, Lumped equivalent circuits of magnetic components: the gyrator-capacitor approach, *IEEE Trans. Power Electron.* **8**, 97 (1993).
- [29] D. Sheahan and H. Orchard, Integratable gyrator using mos and bipolar transistors, *Electron. Lett.* **2**, 390 (1966).
- [30] T. Rao and R. Newcomb, Direct-coupled gyrator suitable for integrated circuits and time variation, *Electron. Lett.* **2**, 250 (1966).

- [31] A. Morse and L. Huelsman, A gyrator realization using operational amplifiers, *IEEE Trans. Circuit Theory* **11**, 277 (1964).
- [32] R. Riordan, Simulated inductors using differential amplifiers, *Electron. Lett.* **3**, 50 (1967).
- [33] A. Antoniou, Gyration using operational amplifiers, *Electron. Lett.* **3**, 350 (1967).
- [34] A. Nikzamid, K. Rouhi, A. Figotin, and F. Capolino, Demonstration of exceptional points of degeneracy in gyrator-based circuit for high-sensitivity applications, [arXiv:2107.00639](https://arxiv.org/abs/2107.00639).
- [35] A. Figotin, Synthesis of lossless electric circuits based on prescribed Jordan forms, *J. Math. Phys.* **61**, 122703 (2020).
- [36] A. Figotin, Perturbations of circuit evolution matrices with Jordan blocks, *J. Math. Phys.* **62**, 042703 (2021).
- [37] M. Ehsani, I. Husain, and M. O. Bilgiç, Power converters as natural gyrators, *IEEE Trans. Circuits Syst., I* **40**, 946 (1993).
- [38] B. Sheno, Practical realization of a gyrator circuit and RC-gyrator filters, *IEEE Trans. Circuit Theory* **12**, 374 (1965).
- [39] W. D. Heiss, Exceptional points of non-Hermitian operators, *J. Phys. A: Math. Gen.* **37**, 2455 (2004).
- [40] H. Kazemi, M. Y. Nada, T. Mealy, A. F. Abdelshafy, and F. Capolino, Exceptional Points of Degeneracy Induced by Linear Time-Periodic Variation, *Phys. Rev. Appl.* **11**, 014007 (2019).
- [41] H. Kazemi, A. Hajiaghajani, M. Y. Nada, M. Dautta, M. Alshetaiwi, P. Tseng, and F. Capolino, Ultra-sensitive radio frequency biosensor at an exceptional point of degeneracy induced by time modulation, *IEEE Sens. J.* **21**, 7250 (2020).
- [42] A. Welters, On explicit recursive formulas in the spectral perturbation analysis of a Jordan block, *SIAM J. Matrix Anal. Appl.* **32**, 1 (2011).
- [43] H. Hodaie, A. U. Hassan, S. Wittek, H. Garcia-Gracia, R. El-Ganainy, D. N. Christodoulides, and M. Khajavikhan, Enhanced sensitivity at higher-order exceptional points, *Nature (London)* **548**, 187 (2017).
- [44] K. Rouhi, H. Kazemi, A. Figotin, and F. Capolino, Exceptional points of degeneracy directly induced by space-time modulation of a single transmission line, *IEEE Antennas Wireless Propag. Lett.*, **19**, 1906 (2020).
- [45] T. Li, W. Wang, and X. Yi, Enhancing the sensitivity of optomechanical mass sensors with a laser in a squeezed state, *Phys. Rev. A* **104**, 013521 (2021).
- [46] R. Azzam, Light-reflection liquid-level sensor, *IEEE Trans. Instrum. Meas.* **29**, 113 (1980).
- [47] B. Yun, N. Chen, and Y. Cui, Highly sensitive liquid-level sensor based on etched fiber Bragg grating, *IEEE Photonics Technol. Lett.* **19**, 1747 (2007).
- [48] E. Vorathin, Z. Hafizi, A. Aizzuddin, M. K. A. Zaini, and K. S. Lim, A novel temperature-insensitive hydrostatic liquid-level sensor using chirped FBG, *IEEE Sens. J.* **19**, 157 (2018).
- [49] S. Khaliq, S. W. James, and R. P. Tatam, Fiber-optic liquid-level sensor using a long-period grating, *Opt. Lett.* **26**, 1224 (2001).
- [50] H. Golnabi, Design and operation of a fiber optic sensor for liquid level detection, *Opt. Lasers Eng.* **41**, 801 (2004).
- [51] X. Lin, L. Ren, Y. Xu, N. Chen, H. Ju, J. Liang, Z. He, E. Qu, B. Hu, and Y. Li, Low-cost multipoint liquid-level sensor with plastic optical fiber, *IEEE Photonics Technol. Lett.* **26**, 1613 (2014).
- [52] V. Sakharov, S. Kuznetsov, B. Zaitsev, I. Kuznetsova, and S. Joshi, Liquid level sensor using ultrasonic Lamb waves, *Ultrasonics* **41**, 319 (2003).
- [53] F. N. Toth, G. C. Meijer, and M. van der Lee, A planar capacitive precision gauge for liquid-level and leakage detection, *IEEE Trans. Instrum. Meas.* **46**, 644 (1997).
- [54] H. Canbolat, A novel level measurement technique using three capacitive sensors for liquids, *IEEE Trans. Instrum. Meas.* **58**, 3762 (2009).
- [55] K. Chetpattananondh, T. Tapoanoi, P. Phukpattaranont, and N. Jindapetch, A self-calibration water level measurement using an interdigital capacitive sensor, *Sens. Actuators, A* **209**, 175 (2014).
- [56] J. R. Hanni and S. K. Venkata, A novel helical electrode type capacitance level sensor for liquid level measurement, *Sens. Actuators, A* **315**, 112283 (2020).
- [57] B. Kumar, G. Rajita, and N. Mandal, A review on capacitive-type sensor for measurement of height of liquid level, *Meas. Control* **47**, 219 (2014).
- [58] K. Loizou and E. Koutroulis, Water level sensing: State of the art review and performance evaluation of a low-cost measurement system, *Measurement* **89**, 204 (2016).
- [59] S. C. Bera, J. K. Ray, and S. Chattopadhyay, A low-cost noncontact capacitance-type level transducer for a conducting liquid, *IEEE Trans. Instrum. Meas.* **55**, 778 (2006).
- [60] E. Terzic, J. Terzic, R. Nagarajah, and M. Alamgir, *A Neural Network Approach to Fluid Quantity Measurement in Dynamic Environments* (Springer, London, 2012).
- [61] N. S. Midi, K. Sasaki, R.-I. Ohyama, and N. Shinyashiki, Broadband complex dielectric constants of water and sodium chloride aqueous solutions with different DC conductivities, *IEEE Trans. Electr. Electron. Eng.* **9**, S8 (2014).